ADVANCED FUNCTIONAL MATERIALS
www.afm-journal.de

Non-Destructive Thermal Evaluation on Laser-Stimulated 3D Functional Nanomembranes via Stokes and Anti-Stokes Raman Scattering

Xiang Dong, Ziyu Zhang, Binmin Wu, Zhi Zheng, Yang Wang, Gaoshan Huang,* and Yongfeng Mei**

3D nanomembranes, defined as freestanding thin films, exhibit unique optical and optoelectronic properties under light or laser illumination due to enhanced light absorption and broad-angle detection. These features enable widespread applications, including passive (e.g., optical microcavities, sensors, metamaterial fibers) and active devices (e.g., phototransistors, bolometers, photodetectors). However, due to low heat capacity and limited thermal dissipation in 3D nanomembranes with tens-of-nanometer thickness, thermal accumulation occurs under laser illumination and often compromises device performance. Here, a systematic, non-destructive thermal evaluation of 3D functional nanomembranes using Stokes and anti-Stokes Raman scattering is presented. Laser-stimulated local temperature is experimentally determined from the Stokes-to-anti-Stokes intensity ratio and validated by finite element simulations. Both experimental and simulation results reveal significant thermal accumulation, with local temperature reaching ≈1300 K under laser irradiation. To manage this thermal effect, laser parameters and ambient conditions are optimized for precise thermal control. By integrating Raman-based measurements with simulations, thermal evaluation and management of 3D nanomembranes, enabling rational design of passive and active devices—such as preventing thermal damage in 3D Si microtube resonators and enhancing response in VO_2-based bolometers, are achieved. This work provides a promising strategy for the thermal design of 3D microdevices in photonics and optoelectronics.

1. Introduction

3D microstructures are emerging as key building blocks for next-generation devices in photonics[1–4] optoelectronics,[5–10] microrobotics,[11] and energy harvesting.[12] For optical and optoelectronic devices, 3D microstructures offer distinct advantages. First, their 3D configuration enables higher integration densities within a compact footprint, which helps reduce device size and power consumption.[13–16] Second, the geometry of 3D structures enables unique light-matter interactions that are unavailable in planar structures.[17,18] For instance, tubular geometries can trap light through multiple internal reflections, thereby increasing light absorption.[19] Third, unlike planar devices that primarily respond to near-normal incidence, 3D architectures interact with oblique and near-parallel incident light, enabling wide-angle detection in advanced photodetectors.[20] Therefore, such 3D devices have been widely fabricated using methods including 3D printing,[21,22] two-photon polymerization,[23] thin-film buckling and transferring,[16,24–27] Among these methods, self-rolling nanomembranes (NMs) have attracted growing interest due to their material versatility—including metals,[28] oxides,[6,16] semiconductors,[8,29] and 2D materials.[5,30] They have been widely applied in both passive and active optical and optoelectronic devices. In the case of passive devices—defined as components that operate without the need for external electronic power—3D rolled-up NMs have been particularly effective as optical filters.[31,32] For example, oxides and silicon-based NMs rolled into tubular geometries can support whispering gallery modes (WGMs) under optical pumping. These WGMs confine light of specific frequencies, enabling wavelength-selective filtering.[32] For active devices requiring external bias, such as photodetectors and bolometers, 3D NMs provide distinct advantages in light absorption and thermal response. For instance, the tubular photodetectors can be fabricated by Te/SiN_x NMs[33] and MoS_2/Oxides NMs,[19] which can achieve wide-angle and polarization-resolved photodetection. Furthermore, the active tubular bolometer can be fabricated by vanadium dioxide (VO_2) NM.[6] With enhanced light absorption and superior thermal insulation due to 3D structures, the VO_2-based bolometer boosts infrared detectivity and temperature sensitivity compared to flat devices.[6] Thus, 3D NM-based

X. Dong, Z. Zhang, B. Wu, Z. Zheng, Y. Wang, G. Huang, Y. Mei
International Institute for Intelligent Nanorobots and Nanosystems and State Key Laboratory of Surface Physics, College of Intelligent Robotics and Advanced Manufacturing
Fudan University
Shanghai 200438, P. R. China
E-mail: wangyang_fd@fudan.edu.cn; gshuang@fudan.edu.cn; yfm@fudan.edu.cn
X. Dong, Z. Zhang, B. Wu, Z. Zheng, Y. Wang, G. Huang, Y. Mei
Yiwu Research Institute of Fudan University
Zhejiang 322000, P. R. China

The ORCID identification number(s) for the author(s) of this article can be found under https://doi.org/10.1002/adfm.202517800

DOI: 10.1002/adfm.202517800

structures provide a versatile platform for optical and optoelectronic devices.[4,34]

Despite their unique optical and optoelectronic properties, 3D rolled-up NMs can experience significant thermal accumulation during operation under light or laser illumination.[35–37] This arises from their low volumetric heat capacity, making them highly susceptible to rapid heating.[6,38] Furthermore, the confined 3D geometry limits heat dissipation, causing localized temperature rise from optical absorption.[35] Such thermal accumulation can easily influence device performance. In some cases, moderate thermal accumulation enhances performance. For instance, the 3D VO_2 bolometer shows improved responsivity with increasing temperature when its temperature stays below the phase transition threshold (≈341K).[6] However, excessive thermal accumulation can degrade both passive and active devices, potentially causing irreversible damage. First, local hotspots induce non-uniform operating conditions and thermal stress, accelerating material fatigue or triggering unwanted phase transitions.[6,39] Second, elevated temperatures affect key material properties—reducing mobility, shifting threshold voltages, and altering emissivity—resulting in unpredictable behavior.[35,40] Third, ultra-high local temperatures can cause melting or irreversible oxidation, directly damaging the device.[35,41] Therefore, precise evaluation of local temperatures in 3D NMs is essential for thermal management and reliable device design.

Accurate temperature evaluation of 3D geometries requires a reliable, high-resolution method tailored for microscale curved surfaces. However, conventional techniques—including thermographic imaging,[42] contact thermometry,[43] and fluorescent methods[44]—were designed for planar surfaces and face major limitations when applied to complex 3D geometries. Infrared thermography offers full-field imaging but is diffraction-limited, with even specialized micro-infrared cameras achieving ≈10 µm resolution.[45] In contrast, laser-induced thermal accumulation typically occurs over regions as small as 1–5 µm.[46] Contact-based methods such as micro-thermocouples and scanning thermal microscopy also face intrinsic limitations. Micro-thermocouples can disturb the system and average temperatures over contact areas,[43] and scanning thermal microscopy struggles to maintain stable contact on curved or freestanding 3D NMs. Moreover, contact-based methods may physically damage fragile 3D NMs. Fluorescent thermometry using embedded dyes or quantum dots enables nanoscale mapping,[44] but introduces foreign materials into the device. These additives may undesirably alter local material properties, such as optical absorption or thermal conductivity.[6,39] So far, conventional methods lack the spatial resolution, geometric adaptability, or non-invasiveness required for 3D microarchitectures. These limitations highlight the urgent need for thermometry techniques compatible with 3D geometries, enabling precise and non-destructive thermal evaluation for next-generation optical and optoelectronic devices.

In this work, we present a thermal evaluation method for functional NMs in laser-stimulated 3D rolled-up geometries. The method combines Stokes and anti-Stokes Raman scattering with finite element method (FEM) simulations. By analyzing the anti-Stokes to Stokes intensity ratio from the intrinsic material, local temperatures on 3D geometries can be measured in a non-contact, non-destructive manner with ≈5 µm resolution.[47] Using this method, we revealed that laser-stimulated 3D architectures can reach local temperatures as high as ≈1300 K. To investigate and mitigate this thermal accumulation, we systematically tuned key laser parameters–spot size, power, and ambient temperature–and correlated the results with FEM simulations. This combined experimental–simulation strategy enables effective thermal management in 3D NMs and supports the design of diverse devices. For passive devices, we studied a 3D silicon NM-based microtube previously used in optical resonators,[32,48] where local temperature was controlled between ≈700 and ≈1300 K. Exceeding 1000 K poses risks of irreversible material degradation, highlighting the need for active thermal regulation. For active devices, we investigated a VO_2 NM-based rolled-up tubular bolometer. Owing to its insulator-to-metal transition at ≈341 K,[6] VO_2 is highly sensitive to temperature variations below this threshold. Local temperature control was achieved by adjusting wall thickness, laser power, and ambient temperature, with Raman results in good agreement with FEM simulations. As a result, we demonstrated a VO_2-based tubular bolometer with enhanced response, highlighting its potential for integration into high-performance infrared imaging systems. Overall, this study offers a non-destructive strategy for thermal evaluation and control of 3D NM-based systems, providing practical guidance for designing thermally robust optical and optoelectronic devices.

2. Result and Discussion

2.1. Fabrication of Rolled-Up Microtubes and Thermal Accumulation Under Illumination

To evaluate laser-induced thermal accumulation in 3D architectures, we employed self-rolled-up microtubes as representative 3D NM structures. These microtubes were fabricated via a strain-engineered self-rolling process, as illustrated in **Figure 1a**. A sacrificial layer and functional NM were deposited sequentially on the substrate, followed by photolithographic patterning and reactive ion etching (RIE) to expose the underlying layer.[8] Selective wet etching released the NM, which rolled up into tubular geometries driven by built-in strain gradients.[5,9] To validate the broad applicability of our non-destructive thermal evaluation approach, we prepared both passive and active device platforms: silicon NM microtubes representing passive components (e.g., optical filters), and VO_2 NM microtubes representing active devices (e.g., bolometers). The silicon NM microtubes were fabricated following the process described in Figure 1a, and the rolled-up microstructures are shown in the SEM image in Figure 1b. For the VO_2 NM microtubes, the fabrication procedure is illustrated in Figure S1 (Supporting Information). A 180 nm-thick VO_2 layer was deposited on thermally oxidized silicon using magnetron sputtering. To introduce a strain gradient, a Cr layer was deposited on top of the VO_2 film, where the difference in thermal expansion coefficients between VO_2 and Cr induced an internal strain gradient during deposition. After removing the patterned SiO_2 sacrificial layer, the VO_2/Cr NM was released and rolled upward into a tubular structure, as shown in Figure S2 (Supporting Information).

Using the constructed microtube structures, we conducted FEM simulations and non-contact Raman thermometry to

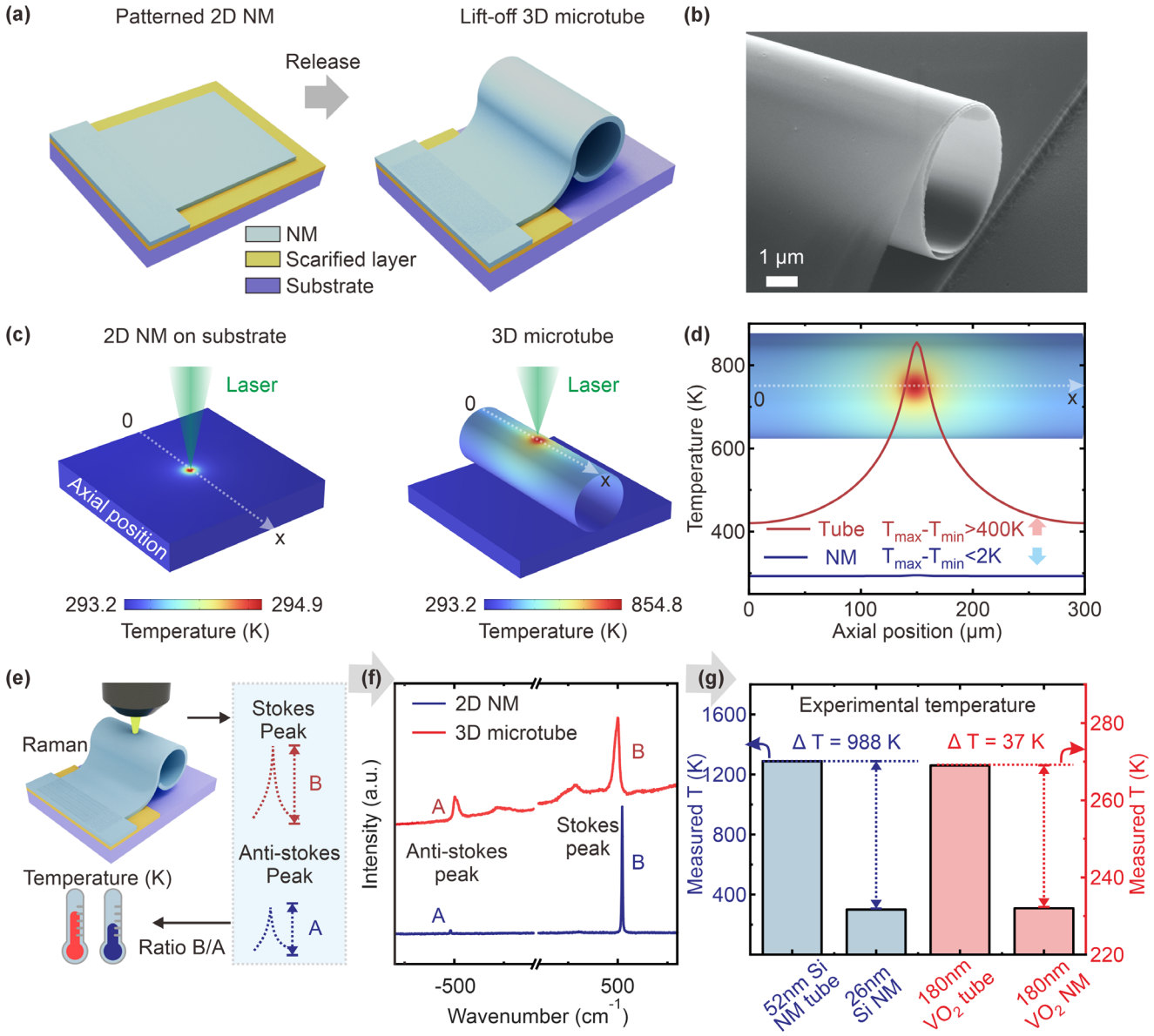

Figure 1. Fabrication of rolled-up microtubes and thermal accumulation of 3D microtubes under laser illumination. a) Schematic illustration of the fabrication process of a rolled-up microtube. A 2D Si NM is patterned on a sacrificial layer deposited on a silicon substrate. Upon selective wet etching of the sacrificial layer, the released Si NM self-rolls into a microtube due to built-in strain. b) SEM image of a fabricated microtube with a radius of ≈4.14 μm and curling number of 2. Scale bar: 1 μm. c) Finite element analysis of temperature distribution under 532 nm laser illumination for a planar 2D nanomembrane (left) and a 3D microtube (right). d) Comparison of the axial temperature profile along the x-direction for the microtube (red) and planar membrane (blue). e) Measurement process of local temperature using Raman spectroscopy. f) Schema of result of Raman spectroscopy with Stokes and Anti-stokes signal. g) Schema of result of local temperature under laser spot obtained from the ratio of Stoke and anti-Stokes intensities.

investigate the thermal behavior of self-rolled Si NM microtubes in comparison with their planar counterparts under laser stimulation. As shown in Figure 1c, we performed FEM simulations to compare the temperature distribution in a planar Si NM and a Si NM microtube under focused 532 nm laser illumination. To exclude the influence of thermal mass, the NMs in both structures were designed with identical thicknesses (50 nm), and the planar NM had a patterned area of 300 μm × 300 μm, while the microtube was formed by rolling the same NM into a single turn with a diameter of ≈95 μm. Under 10 mW laser illumination, the planar Si NM exhibited moderate local heating, with the maximum temperature increased to ≈295 K near the laser spot. In contrast, the 3D microtube showed a significantly higher local temperature rise, with the peak temperature reaching ≈855 K under the same irradiation conditions. To quantitatively evaluate this difference, we analyzed the temperature distribution along the axial direction (indicated by the white dashed lines in Figure 1c), and the corresponding profiles are shown in Figure 1d. The microtube exhibited not only a generally higher temperature across the axial direction compared to the planar

NM, but also a much greater temperature gradient. Specifically, the temperature difference between the hottest and coolest points in the microtube exceeded 400 K, while that in the planar structure was less than 2 K. This obvious thermal accumulation in the microtube is primarily attributed to the fundamentally different heat dissipation mechanisms.[6] In the planar configuration, the NM is in direct contact with the underlying substrate, providing an efficient thermal conduction pathway that rapidly dissipates heat. In contrast, the microtube is surrounded by air, which has an extremely low thermal conductivity (≈0.025 $W{\cdot}m^{-1}{\cdot}K^{-1}$). As a result, heat generated by laser irradiation cannot be effectively dissipated, leading to localized thermal buildup with temperature rises exceeding 400 K.

To experimentally assess localized thermal accumulation in laser-stimulated 3D functional nanomembranes, we established a non-destructive temperature measurement method based on Stokes and anti-Stokes Raman scattering, as illustrated in Figure 1e. A 532 nm laser simultaneously served as the excitation source and local heating input. Raman spectra were thus collected from the microtube using a low-wavenumber notch filter to capture both Stokes and anti-Stokes signals, which arise from inelastic photon-phonon interactions reflecting the material's vibrational energy exchange.[49] Because the anti-Stokes process depends on the thermal population of vibrational states, its intensity relative to the Stokes signal follows the Boltzmann distribution.[50] This temperature dependence makes the Stokes-to-anti-Stokes intensity ratio a reliable, non-contact probe for quantifying local temperature in 3D NMs. Furthermore, the spatial resolution of this method is determined by the laser spot size of the Raman microscope. With a 100× objective lens, the focused laser spot diameter can be reduced to below 5 µm. This spatial precision surpasses that of conventional infrared thermography, offering a powerful tool for investigating thermal behavior in microarchitectures.

Using this measurement approach, we compared 2D Si NM with 3D Si microtube under 3.65 mW laser illumination. Raman spectra in Figure 1f show both Stokes and anti-Stokes peaks, and the 3D tubular structure exhibits a significantly stronger anti-Stokes signal than the 2D NM, indicating a higher local temperature due to pronounced thermal accumulation in the 3D geometry. The temperature T was extracted using the intensity ratio of anti-Stokes to Stokes peaks, following the Boltzmann-distribution-governed relation:[49,50]

$$\frac{I_{As}}{I_s} = \frac{\omega_{As}^4}{\omega_S^4} e^{-\frac{\hbar\omega}{K_b T}} \tag{1}$$

where I_S,I_{As} stand for intensities of Stokes and anti-Stokes peak, ω_S,ω_{AS} is the wavelength of Stokes and anti-Stokes peak,$\hbar$ is the reduced Planck constant, ω is the excitation laser wavelength, K_b is Boltzmann constant, T is the temperature. In this situation, all variables remain constant except temperature T so ratio $\frac{I_{As}}{I_s}$ is related directly to T and we can rewrite this equation as:

$$T_{measurement} = \frac{2\pi\hbar\omega}{K_b \ln\left[A\frac{I_{SE}}{I_{AsE}}\left(\frac{\omega_{As}}{\omega_s}\right)^4\right]} \tag{2}$$

Here we add a factor A for extra Sokes/anti-Stokes intensity ratio introduced by the measurement system (Figure S3, Supporting Information; Section 2.2 for the detail calibration). This factor can be determined by $A = \frac{I_{SE} I_{As}}{I_{AsE} I_S}$, where I_{SE}, I_{AsE} stands for the Stokes and Anti-stokes peak measured in an experiment at a certain temperature. After calibrating the factor A, we can process the measurement and get the local temperature for different structures (Figure 1g). For the 3D Si microtubes, the maximum measured local temperature reaches ≈1288 K, whereas for the planar 2D Si NM, the corresponding temperature at ≈300 K. This substantial temperature difference of 988 K provides direct evidence of pronounced thermal accumulation in the tubular geometry. Such localized heating can be effectively managed by tuning the NM thickness, adjusting laser parameters, or modifying the ambient temperature. For example, under laser irradiation at a power of 0.1 mW, 180 nm-thick VO_2 NM microtubes exhibit a local temperature of 269 K when measured at a base temperature of 173 K, while 2D VO_2 NMs with the same thickness only reach 232 K under irradiation at a base temperature of 231 K. These experimental and simulation results demonstrate the effectiveness of our contact-free thermal probing strategy for 3D architectures and highlight its value for guiding the design of thermally robust photonic and optoelectronic devices.

2.2. Temperature Measurement and Calibration Model via Stokes and Anti-Stokes Raman Spectroscopy

As described in Figure 1, our Raman-based thermal evaluation enables non-contact temperature measurement of 3D microstructures. However, accurate temperature calibration during experimental measurements is technically challenging due to inherent system errors in the Raman setup (Figure S3, Supporting Information). These errors primarily originate from wavelength-dependent transmission differences in optical components such as lenses, varying sensitivity of the CCD detector to different wavelengths, and inconsistencies in objective lens focusing conditions. To correct for these factors, we employed a planar 2D Si NM—which exhibits negligible laser-induced heating (<2 K)—as a calibration reference. As shown in **Figure 2a**, the 2D Si NM was mounted on a temperature-controlled stage and probed with low-power (0.1 mW) laser excitation, which resulted in an extremely small increase in local temperature (< 0.1 K, Figure S4, Supporting Information). By gradually increasing the stage temperature from 50 to 300 °C, we acquired Raman spectra at different thermal states. The anti-Stokes intensity increased systematically with temperature, governed by the Boltzmann population of vibrational states. Lorentzian fitting of the Stokes and anti-Stokes peaks enabled us to extract their intensities and positions. As seen in Figure 2b, the Stokes peak redshifted from 521 cm^{-1} to 515 cm^{-1}, primarily due to anharmonic phonon interactions and lattice expansion, particularly involving three-phonon and four-phonon interactions.[50] Meanwhile, we also investigated the ratio of Stokes to anti-Stokes peak intensities at different stage temperatures. For each temperature point, five independent measurements were performed and averaged to ensure accuracy, and the results are presented in Figure 2c. It can be observed that the peak ratio decreases rapidly with increasing heater stage temperature. This trend is consistent with the theoretical prediction described by Equation (1), where $\frac{I_{As}}{I_s} \propto e^{-\frac{\hbar\omega}{K_b T}}$; thus, as the temperature increases, the exponential term decreases rapidly.

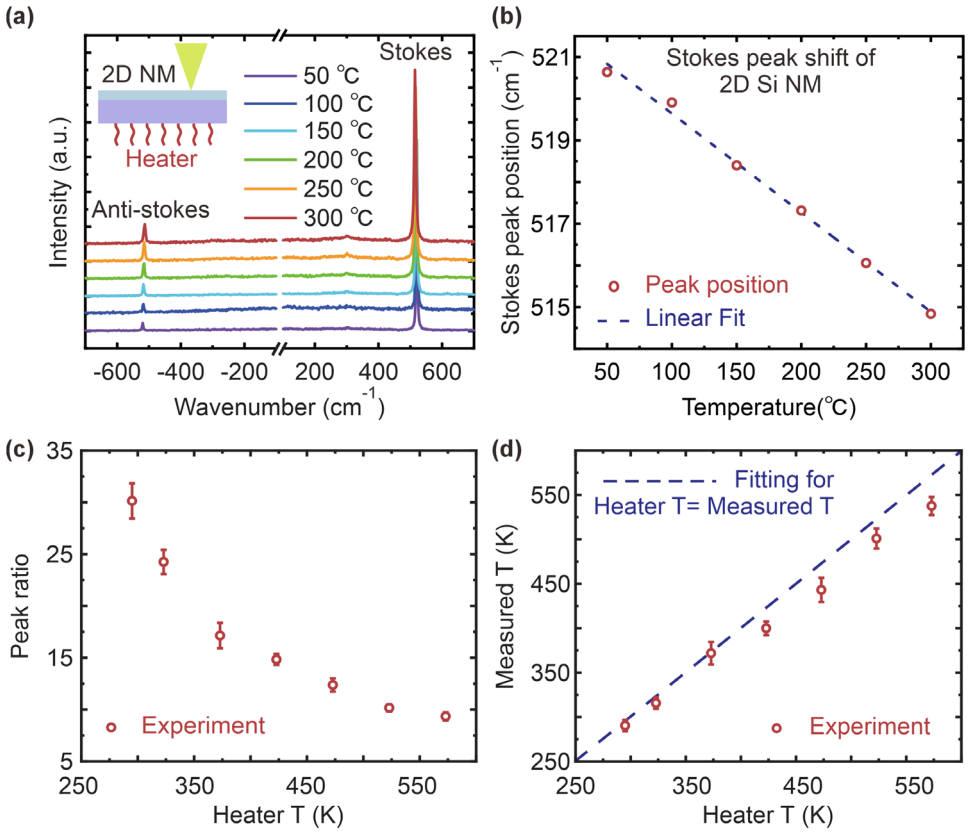

Figure 2. Raman-based temperature calibration using a 2D Si NM. a) Raman spectra of a planar Si nanomembrane at different temperatures (50–300 °C) using a temperature-controlled heating stage. b) Stokes peak position shift of different temperature c) Extracted peak intensity ratios as a function of heater temperature. d) Correlation between measured Raman temperature and heater-set temperature. The dashed blue line indicates the ideal linear relation $T_{measurement} = T_{heater}$.

Based on the extracted Stokes and anti-Stokes peak positions and intensity ratios, we performed a temperature calibration of the Raman system and determined the absolute local temperature. At a reference temperature of 296 K, the calibration factor A was calculated to account for instrumental asymmetries, including CCD sensitivity and optical transmission. Using this factor and the Boltzmann-governed intensity ratio, we accurately extracted the local temperature from Raman spectra, as described by Equation (2). As shown in Figure 2d, the measured temperatures align closely with the heating stage setpoints, confirming the validity of our calibration. Minor deviations stem from thermal gradients across the NM-substrate interface. These results verify that the non-destructive, Raman-based thermal evaluation approach enables precise local temperature mapping, establishing a robust foundation for applications in laser-stimulated 3D functional nanomembranes.

2.3. Thermal Evaluation and Management of Passive 3D Microtube Device

We further investigated the thermal accumulation behavior and its management in 3D microtube devices. Depending on whether the devices are externally powered, microtubular devices can be categorized as passive or active. For passive devices, silicon-based microtubes have been widely utilized in optical sensors and optical filters. Therefore, the Si NM microtube was selected as a representative example of typical passive 3D devices. We characterized and managed the thermal accumulation in Si NM microtubes, as shown in **Figure 3**. A focused laser beam with a constant power of 3.65 mW was directed onto 3D microtube surface, serving simultaneously as both the heat source and the probing light. By tuning the laser expansion parameter, we systematically adjusted the diameter of the focused laser spot; the linear relationship between the spot expansion setting and the actual spot size is shown in Figure S5 (Supporting Information). Raman spectra of 3D Si microtubes under different focused laser spot diameters were measured and are presented in Figure 3a.

As shown in Figure 3a, with the decrease in laser spot size (indicated by the gray arrow), the anti-Stokes peak in the Raman spectra gradually becomes more pronounced, indicating a temperature rise in the illuminated region of the 3D Si NM microtube. This temperature increase results from the enhanced laser power density caused by the reduced spot size, despite the total laser power remaining constant. The higher power density leads to an increased heat flux per unit area, thereby raising the local temperature. By analyzing both the Stokes and anti-Stokes peak positions and intensities using Lorentzian fitting (Figure 3a), we obtained the corresponding spectral parameters under different laser spot expansion settings. A comparison of the Stokes

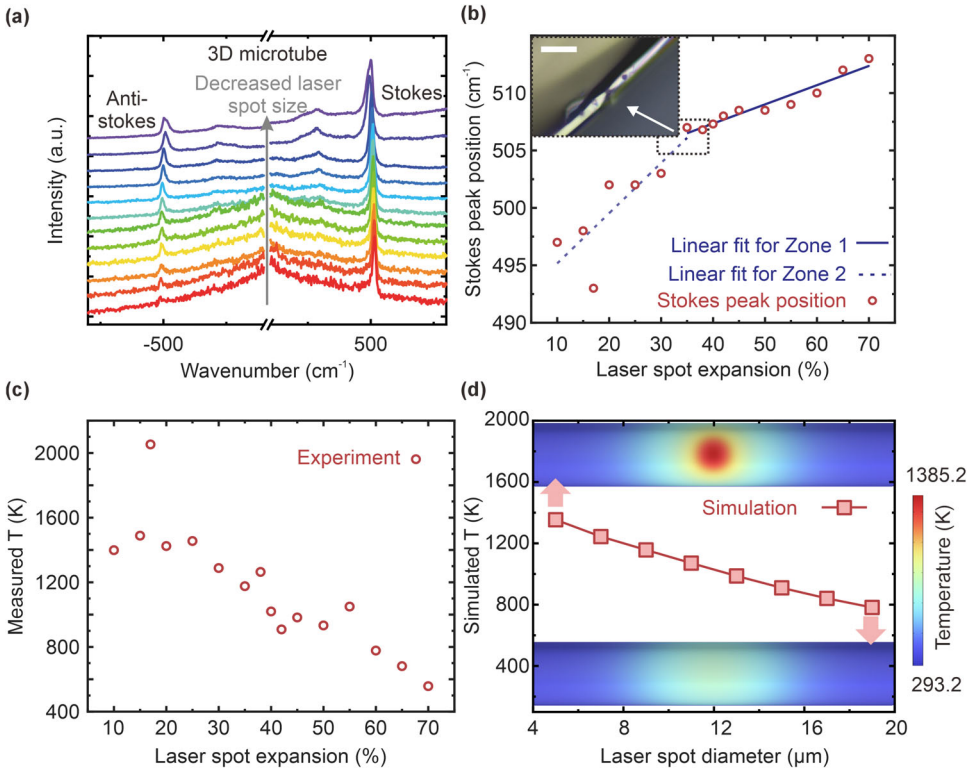

Figure 3. Thermal accumulation and management on 3D Si microtubes. a) Raman spectra of the 3D microtube under varying laser spot sizes. b) Evolution of the Stokes peak position as a function of laser spot expansion. Two zones with a turning point where the tube is damaged are fitted separately. c) Experimentally measured local temperature under different laser spot expansions. d) Simulated temperature profiles as a function of laser spot diameter.

peak positions with the spot expansion values reveals two distinct regimes, as shown in Figure 3b. Initially, as the laser spot expansion decreases, the Stokes peak exhibits a redshift, consistent with the temperature-dependent softening of phonon modes observed in 2D Si NMs (Figure 2b). However, we observed that the relationship between the Stokes peak position and the spot expansion can be divided into two distinct linear regimes, defined as Zone 1 (35–70%) and Zone 2 (10–35%). This behavior can be interpreted based on the fundamental relationship between Raman peak position, temperature, and stress. As described by Equation (3), the Raman peak shift ($\Delta\omega$) is influenced by both thermal and stress-induced effects:[50]

$$\Delta\omega = A_i \Delta T + K\Delta\sigma \tag{3}$$

where $\Delta\omega$ is the Raman peak shift, A_i is the temperature-Raman shift coefficient, ΔT is the temperature change. K is the stress-Raman shift coefficient. $\Delta\sigma$ is the stress variation. In Zone 1, where the laser expansion exceeds 35%, the material remains structurally intact without signs of degradation, melting, or oxidation. In this regime, the peak shift is linearly dominated by temperature-induced changes. In contrast, in Zone 2 (expansion below 35%), a significant increase in the slope of the linear fit suggests that the peak shift is governed by both temperature and stress. This shift is attributed to thermally induced structural deformation of the microtube and the melting and oxidation of Si NM, which alters the local stress state and changes the effective value of A_i. This transition is also clearly visible under optical microscopy: near the boundary between Zone 1 and Zone 2 (≈35%), the Si microtube exhibits obvious collapse and structural damage in the irradiated center region (insets in Figure 3b). Furthermore, we calculated the local temperature using Equation (1) and the intensity ratio of the Stokes and anti-Stokes peaks obtained in Figure 3a (details provided in Figure S6, Supporting Information). The resulting temperature values are plotted in Figure 3c. As shown, the temperature increases approximately linearly as the laser spot expansion decreases. Structural damage to the microtube begins when the local temperature reaches ≈1200 K, and under continued increase in power density, the temperature can rise further to ≈1500 K under a total laser power of 3.65 mW.

To further investigate this phenomenon, we performed FEM simulations by varying the laser spot diameter from 5 to 18 μm while keeping the total laser power constant. The resulting temperature distributions are shown in Figure 3d and Figure S7 (Supporting Information). As the spot diameter increases, the average temperature in the irradiated region decreases significantly—from ≈1400 K down to ≈800 K—in good agreement with the experimental measurements. The slight discrepancy between experiment and simulation mainly arises from curvature-induced optical effects and additional heat dissipation pathways. In addition to laser spot size control, thermal accumulation in 3D Si microtubes can be effectively managed by adjusting the laser power and NM thickness, as shown in Figure S8

(Supporting Information). For example, simulation results show that when the laser power is reduced from 5 to 1 mW, the maximum temperature drops sharply from ≈1800 to ≈600 K (Figure S9, Supporting Information). Similarly, increasing the Si NM thickness from 50 to 150 nm results in a reduction of the peak temperature from ≈1400 to ≈700 K, as shown in Figure S10 (Supporting Information).

In summary, for 3D Si microtubes functioning as passive microstructures, we confirm that localized thermal accumulation can reach temperatures exceeding 1500 K under focused laser illumination. Once the local temperature exceeds ≈1200 K, thermal degradation of the Si NM surface or structural collapse of the microtube may occur. However, by precisely tuning laser focusing parameters and applying our Raman-based temperature measurement method, we demonstrate that the local temperature can be controlled and maintained ≈600 K. This thermal management strategy provides practical guidance for the design and optimization of passive 3D microtube devices, helping to prevent laser-induced structural damage.

2.4. Thermal Evaluation and Management of VO_2 Microtubes as Active 3D Bolometers

For active devices that require external electrical power, we investigated a VO_2-based bolometer as a representative example. VO_2 is a well-known phase transition material exhibiting strong temperature sensitivity, as illustrated in **Figure 4a**. Below 341 K, VO_2 exists in a monoclinic crystal structure (space group $P2_1/c$) and behaves as an electrical insulator. Between ≈293 and ≈320K, its electrical resistance decreases linearly with increasing temperature, making it suitable for use in active bolometric applications where temperature-dependent resistance is essential. As the temperature exceeds ≈341 K, VO_2 undergoes a sharp metal–insulator transition (MIT), accompanied by a structural phase transformation from the monoclinic phase to the high-temperature rutile phase ($P4_2/mnm$). This transition is not only associated with a dramatic drop in electrical resistance but also involves significant lattice strain, which can induce macroscopic deformation in 3D VO_2 structures. Therefore, VO_2 in this regime is more suitable for applications in microrobots or actuators. However, above ≈920 K in ambient air, VO_2 irreversibly oxidizes to V_2O_5, resulting in permanent degradation of device performance.[39] Hence, precise thermal control is critical for VO_2-based active bolometers to ensure that the device remains within the monoclinic phase during operation.

However, due to the inherently low thermal conductivity of VO_2 (≈5 $W{\cdot}m^{-1}{\cdot}K^{-1}$), compared with silicon (≈148 $W{\cdot}m^{-1}{\cdot}K^{-1}$ at 293 K and ≈19 $W{\cdot}m^{-1}{\cdot}K^{-1}$ at 1500 K),[51] VO_2-based 3D microtubes are significantly more susceptible to thermal accumulation under the same heat flux and geometric conditions. As shown in Figure 4b, FEM simulations reveal that while the maximum temperature in a silicon microtube remains below ≈400 K under laser irradiation, the temperature in a VO_2 microtube under identical conditions can exceed 1400 K. This level of heating is sufficient to trigger irreversible oxidation to V_2O_5 and causes permanent device failure. Therefore, it is crucial to implement systematic thermal regulation strategies for VO_2-based active devices.

We first explored structural tuning through FEM simulations, focusing on wall thickness effects. As shown in Figure 4c, increasing the VO_2 tube wall thickness from 60 to 200 nm effectively suppresses thermal accumulation, reducing the peak temperature from ≈1400 to ≈600 K. This thermal shift moves the material out of the irreversible oxidation regime (Mode A) and into the rutile phase region (Mode B). The underlying mechanism is attributed to the increase in thermal mass and heat dissipation with thicker structures. Such a thickness increase can be achieved either by depositing thicker VO_2 NMs or by designing planar VO_2 patterns that form more rolled-up turns during fabrication. Laser power modulation offers another effective method of thermal control. As shown in Figure 4d, reducing the laser power from 2 to 0.072 mW decreases the peak temperature from ≈933 to ≈316 K, thus stabilizing VO_2 in the monoclinic phase (Mode C). However, even a slight increase in power to ≈0.2 mW can elevate the temperature to ≈357 K, exceeding the MIT threshold and driving the material into the rutile phase. This makes precise power control essential for maintaining VO_2 in its insulating state, which is critical for bolometric operation. In addition, we propose ambient temperature regulation as a complementary thermal management strategy. As demonstrated in Figure 4e, lowering the background temperature from 320 to 200 K reduces the VO_2 microtube's local temperature from ≈368 K (rutile phase, Mode B) to ≈248 K (monoclinic phase, Mode A), providing another avenue for preserving phase stability.

Based on simulation insights, we fabricated 3D VO_2 microtubes and demonstrated their functionality as active bolometric devices, as illustrated in **Figure 5a**. 180 nm-thick VO_2 films were deposited on Si/SiO_2 substrates via magnetron sputtering, and their layered structure was confirmed by cross-sectional TEM (Figure S11, Supporting Information). By patterning a Cr stressor layer partially overlapping the VO_2 film, we induced controlled self-rolling to form tubular geometries. To evaluate the thermal behavior of the 3D VO_2 microtubes, we conducted a comparative study with 2D planar VO_2 NMs. As shown in Figure 5b, Raman spectra of the 2D VO_2 NM at room temperature (293 K) exhibit two prominent peaks at ≈196 and ≈224 cm^{-1}, corresponding to Ag vibrational modes of V – V bonds in the monoclinic phase.[52] With increasing background temperature to 348 K, both Stokes and anti-Stokes peaks gradually diminish and eventually vanish, consistent with the phase transition from the monoclinic (M) to rutile (R) phase of VO_2, which lacks Raman-active modes (Figure S12, Supporting Information).[52]

In contrast, 3D VO_2 microtubes measured at 293 K exhibited no detectable Raman peaks, indicating that thermal accumulation in the tubular geometry had already induced a phase transition to the rutile state. To investigate this further, we systematically lowered the background temperature. At 263 K, weak Stokes peaks began to emerge, and at 213 K both Stokes and anti-Stokes peaks became clearly visible, indicating a complete transition back to the monoclinic phase. By fitting the Raman peaks and applying Equation (1) after system calibration, we extracted the local tube temperature to be ≈297 K at a background of 213 K. At a lower base temperature of 173 K, the local temperature was estimated to be ≈269 K, suggesting a ≈28 K difference from the base, likely caused by convective disturbances from nitrogen flow during cooling. To validate these findings, we conducted FEM simulations to map the relationship between laser

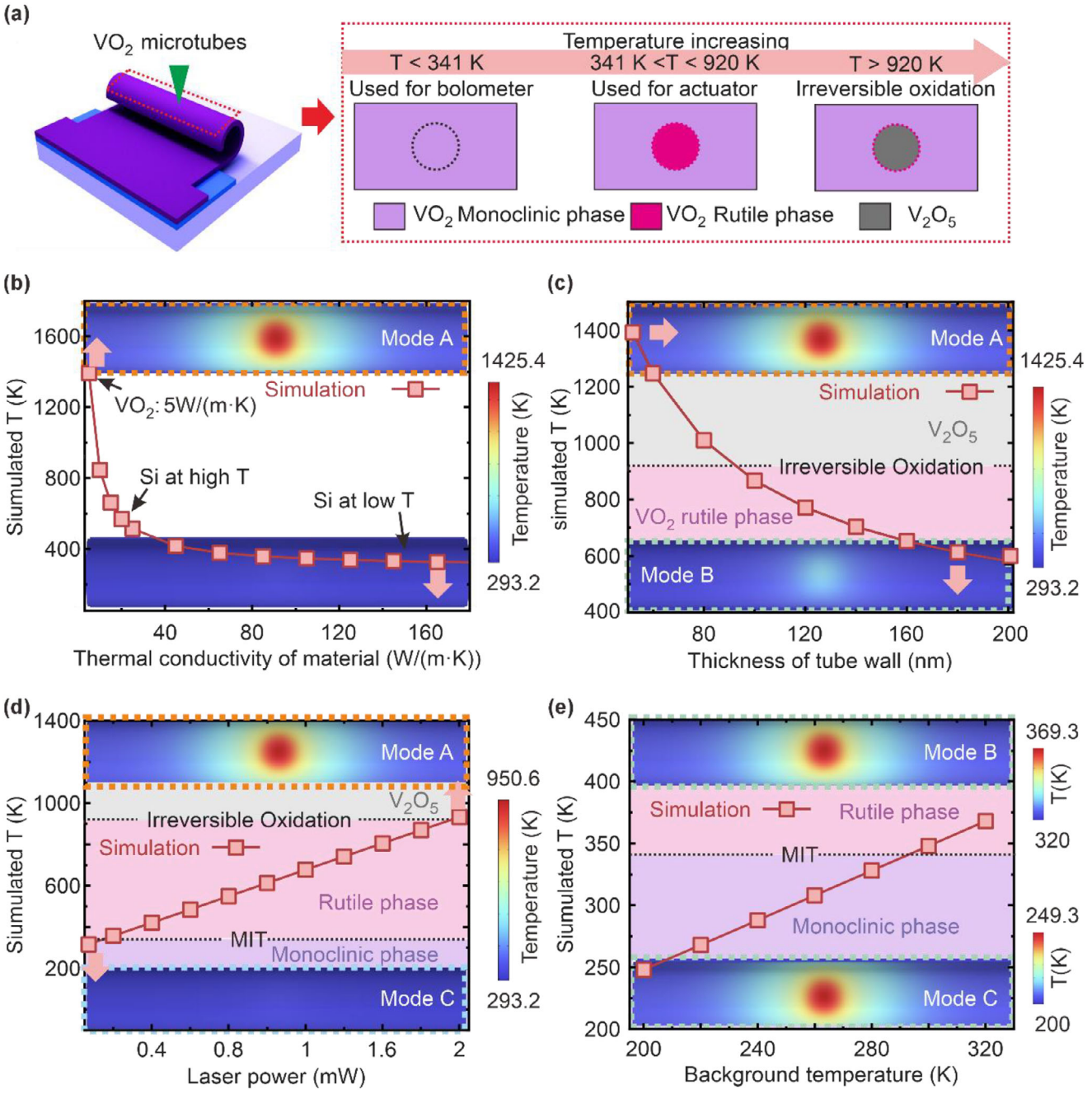

Figure 4. Thermal characteristics and simulation of local heating in a 3D VO_2 microtube bolometer structure. a) Schematic illustration of the VO_2 phase-state changes under increasing temperature: below ≈341 K the VO_2 remains in the monoclinic (insulating) phase with a linear temperature–resistance dependence (operational bolometer regime); between ≈341 K and elevated temperatures (up to ≈10^3 K) the material undergoes an insulator-to-metal phase transition into the rutile phase; at higher temperatures the VO_2 structure is damaged. b–e) FEM of the microtube's local temperature rise as a function of various parameters: (b) material thermal conductivity (comparing a high thermal conductivity Si microtube versus a low thermal conductivity VO_2 microtube under identical laser power), (c) nanomembrane wall thickness, (d) incident laser power, and (e) ambient (base) temperature.

power, background temperature, and resulting VO_2 tube temperature, as shown in Figure 5c. The white contour line represents the M–R phase boundary. Experimentally measured phase states are overlaid: red squares correspond to the monoclinic phase and blue squares to the rutile phase. The experimental data closely match the simulation predictions. From this, we determine that under ambient conditions (293 K), the operational laser power for VO_2 microtubes must remain below ≈0.05 mW to prevent phase transition—critical for bolometer design.

To realize bolometric functionality, interdigital electrodes were patterned on the VO_2 film (160 nm thick) prior to rolling, yielding a 3D tubular VO_2 bolometer (Figure 5d, inset: optical image).

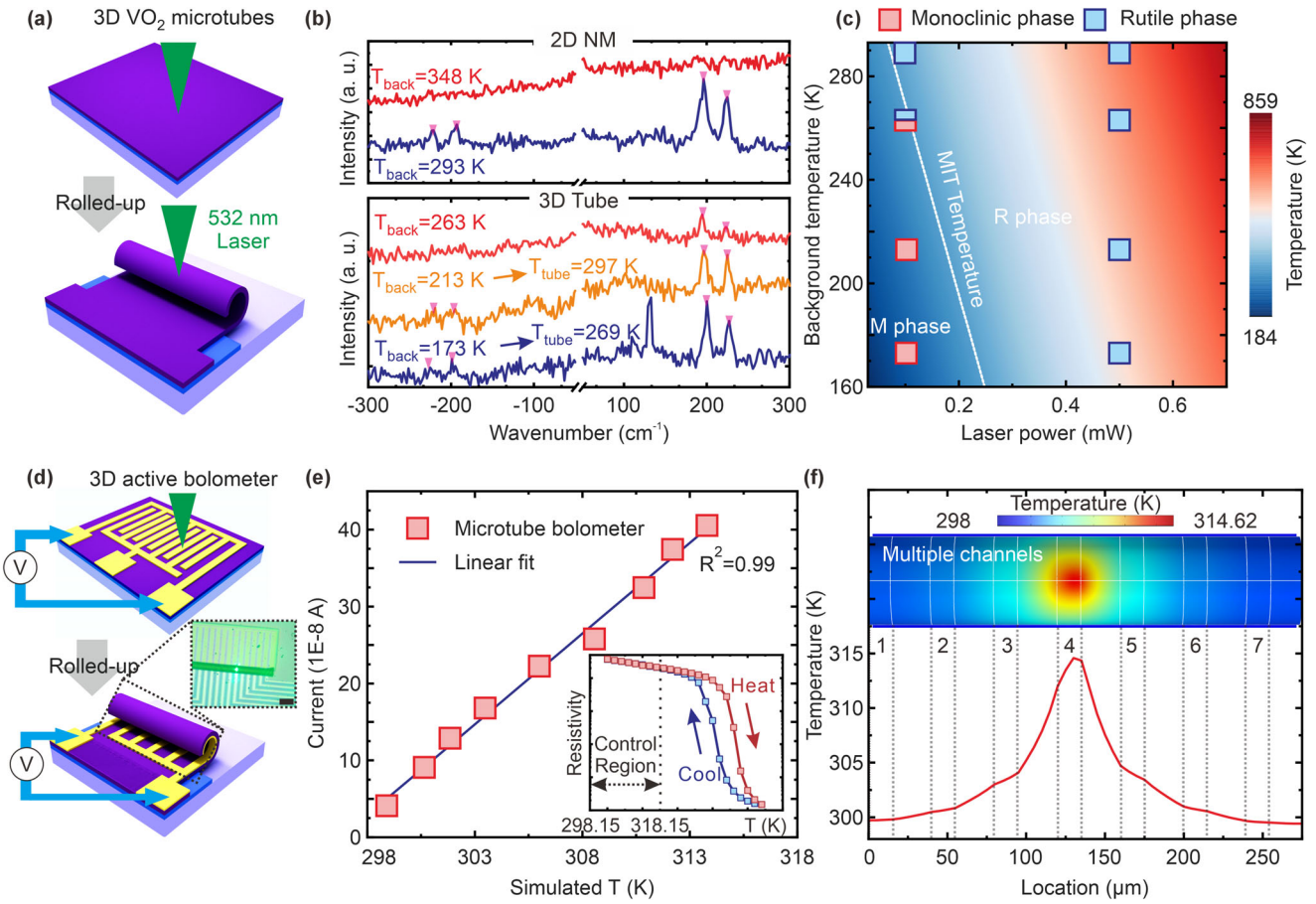

Figure 5. Experimental thermal evaluation and management of 3D VO_2 microtubes for active bolometer applications. a) Schema of VO_2 Raman test on microtube structure. b) Raman spectroscopy of VO_2 2D NM and 3D microtube at different temperatures. c) The simulated temperature of different background temperature and laser power, blue and red points show the experiment data of VO_2 microtube and their corresponding phase. d) Schema of infrared photoelectricity test for tubular bolometer. e) Output current of 3D tube bolometer operating in work temperature with increased 940 nm laser power, the inset show the controlled region for work temperature. f) Simulation of temperature distribution along axis of 3D tube bolometer with electrodes. Scale bars in (d), 100 μm.

The I–V characteristics, confirming device stability, are shown in Figure S13 (Supporting Information). At 298 K, we compared planar VO_2 devices with 3D tubular counterparts (Figure S14, Supporting Information). The microtubes exhibited a clear photocurrent response that scaled with laser intensity, highlighting the role of thermal localization in enhancing responsivity. Nevertheless, as shown in Figure 4, excessive thermal accumulation can drive the device into nonlinear operation. To ensure stable performance, we correlated laser power with local temperature using simulations (Figure 5c; Figure S15, Supporting Information) and resistance–temperature measurements (Figure S16, Supporting Information), thereby defining an operating window between 298 and 318 K (inset of Figure 5e). Within this regime, both the local temperature and the net photocurrent increased linearly with power (Figure 5e). At a high incident power of 55 μW, the VO_2 bolometer exhibited an enhanced photocurrent response. These results confirm that Raman-based temperature mapping enabled effective thermal regulation, allowing VO_2 to remain in the monoclinic phase during bolometric operation and enhancing the IR photoresponse. Finally, to explore the implications for thermal imaging, we simulated the spatial temperature distribution in the microtube upon laser irradiation (Figure 5f). The simulation revealed localized temperature increases near the center of the structure (≈341 K), while the surrounding channels remained significantly cooler, enabling spatially resolved IR detection. These results highlight the unique advantage of our Raman-based thermal management method in both tuning and calibrating VO_2-based bolometric devices and offer a promising path toward the development of high-resolution 3D thermal imaging systems.

3. Conclusion

In this work, we developed a non-destructive, high-resolution thermal evaluation strategy for 3D rolled-up NM structures under laser stimulation. By combining anti-Stokes to Stokes Raman scattering analysis with FEM simulations, we achieved localized, contact-free temperature mapping on curved 3D geometries with high spatial resolution. Experimental results revealed significant thermal accumulation in 3D microtubes, with local temperatures rising up to ≈1300 K—substantially higher than in planar counterparts. For passive devices, we demonstrated temperature

control from ≈700 to 1300 K in silicon NM-based microtubes, where exceeding 1200 K poses a risk of irreversible material degradation. For active devices, we realized phase-sensitive thermal modulation in VO_2 NM-based tubular bolometers near the 341 K metal-to-insulator transition, enabling enhanced response. This Raman-based strategy is broadly applicable to 3D NMs composed of diverse functional materials—including 2D materials, III–V semiconductors, and perovskites—owing to the intrinsic nature of Raman scattering, which requires no contact probes or surface modifications. The technique also offers a powerful platform for precise thermal management in next-generation 3D optoelectronic and photonic microsystems, where thermal accumulation can lead to nonlinear optical effects, phase instability, and degraded device performance.

4. Experimental Section

Si Microtube Fabrication: A solid-source molecular beam epitaxy (MBE) system was used to grow the 40 nm Ge epi-layer followed by a Si epi layer with thickness of 30 nm. The growth is pricess under temperature of 280 °C. The epitaxial Si layer was cleaned by hydrofluoric acid (HF) to remove the oxide layer on its surface. The etching window is defined by photolithography using the following steps: 1) photoresist with 2 µm thickness is coated on the cleaned Si layer. 2) the pattern is developed then exposed under reactive ion etching(RIE) for 40s (35 sccm SF_8 and 18 sccm CHF_3 flow, 30m Torr chamber pressure, 50 W etching power) to create an etching window. 3) The photoresistor is removed by acetone then the sample is steep in 30%H_2O_2 solution at 70 °C for 15 min to remove the sacrifice layer (Ge layer) enable the Si nanomembrane released from the substrate and the stress will make the released film rolled up itself. 4) Critical point dryer (CPD) was used to dry the microtube.

VO_2 Microtube Fabrication: A magnetron sputtering system was used to deposit the polycrystalline VO_2 layer directly on Silicon substrate with oxide layer cleaned with acetone and deionized water. The deposition is under 500 °C for 1800 s in argon–oxygen flow, with 15 mtorr Campman pressure, and the rate of oxygen–argon is 5% and the sputtering power is 200 W, then a Cr layer is deposited by electron beam evaporator to introduce extra stress. The microtube rolled up process is similar to Si microtube, the electrodes were defined by photolithography and the etching window is etched by RIE for 100 s with 30 sccm Ar flow and 30sccm CF_4 flow. The release step use HF to remove the sacrifice layer (SiO_2).

Raman Spectroscopy Measurement: A RENISHAW InVia Qontor Raman system is used to process the measurement. Before every test the Si wafer was used to calibration the system by set the Si peak to 520.5 cm^{-1} and ensure the center of laser spot stay on the center of view under the microscope. Before low wave test, a Low Wavenumber Notch Filter and a slit was used to filter the Rayleigh scattering. Before every Stokes and anti-Stokes test on microtube the Raman spectroscopy of Si wafer was obtained using a laser power of 1% (≈0.1 mW) in room temperature(297K) to find its Stokes-Anti-stokes ratio and contrast with the calculated ratio under this temperature to calibrate the extra ratio caused by the system. The precise heating stage for controlling the temperature is the Linkam THMSG600 Temperature Controlled Geology Stage.

Supporting Information

Supporting Information is available from the Wiley Online Library or from the author.

Acknowledgements

This work was supported by National Key Technologies R&D Program of China (2021YFA0715302, G.H.), National Natural Science Foundation of China (62375054, Y.M. and 523B2107, Z.Z.), Science and Technology Commission of Shanghai Municipality (24520750200, Y.M., 24CL2900202, Y.M., and 25CL2900202, Y.M.), and Shanghai Talent Programs. Part of the experimental work was carried out in the Fudan Nanofabrication Laboratory. The computations in this research were performed using the Computing for the Future at Fudan platform of Fudan University.

Conflict of Interest

The authors declare no conflict of interest.

Data Availability Statement

The data that support the findings of this study are available from the corresponding author upon reasonable request.

Keywords

3D geometry, functional nanomembranes, Raman analysis, thermal evaluation

Received: July 11, 2025
Revised: August 30, 2025
Published online:

[1] S. Chen, Z. Liu, H. Du, C. Tang, C.-Y. Ji, B. Quan, R. Pan, L. Yang, X. Li, C. Gu, X. Zhang, Y. Yao, J. Li, N. X. Fang, J. Li, *Nat. Commun.* **2021**, *12*, 1299.
[2] Z. Liu, H. Du, J. Li, L. Lu, Z.-Y. Li, N. X. Fang, *Sci. Adv.* **2018**, *4*, aat4436.
[3] L. Wang, Z. Tian, B. Zhang, B. Xu, T. Wang, Y. Wang, S. Li, Z. Di, Y. Mei, *Small* **2019**, *15*, 1805477.
[4] H. Dong, C. N. Saggau, M. Zhu, J. Liang, S. Duan, X. Wang, H. Tang, Y. Yin, X. Wang, J. Wang, C. Zhang, Y. S. Zhao, L. Ma, O. G. Schmidt, *Adv. Funct. Mater.* **2021**, *31*, 2109080.
[5] Z. Zhang, T. Cai, Z. Li, B. Wu, Z. Zheng, C. You, G. Jiang, M. Ma, Z. Xu, C. Shen, X. Chen, E. Song, J. Cui, G. Huang, Y. Mei, *Adv. Mater.* **2025**, *37*, 2413771.
[6] B. Wu, Z. Zhang, B. Chen, Z. Zheng, C. You, C. Liu, X. Li, J. Wang, Y. Wang, E. Song, J. Cui, Z. An, G. Huang, Y. Mei, *Sci. Adv.* **2023**, *9*, adi7805.
[7] T. Kim, M. Kim, Y. Jung, H. Jang, C. Dagdeviren, H. Pao, S. Cho, A. Carlson, K. Yu, A. Ameen, H. Chung, S. Jin, Z. Ma, J. A. Rogers, *Chem. Mater.* **2014**, *26*, 3502.
[8] T. Kim, Y. Jung, H. Chung, K. Yu, N. Ahmed, C. Corcoran, J. Park, S. Jin, J. A. Rogers, *Appl. Phys. Lett.* **2013**, *102*, 182104.
[9] K. Zhang, Y. H. Jung, S. Mikael, J.-H. Seo, M. Kim, H. Mi, H. Zhou, Z. Xia, W. Zhou, S. Gong, Z. Ma, *Nat. Commun.* **2017**, *8*, 1782.
[10] B. Wu, Z. Zhang, Z. Zheng, T. Cai, C. You, C. Liu, X. Li, Y. Wang, J. Wang, H. Li, E. Song, J. Cui, G. Huang, Y. Mei, *Adv. Mater.* **2023**, *35*, 2306715.
[11] Y. Wang, X. Li, C. Liu, Y. Wang, C. You, H. Zhu, Z. Zheng, Z. Zhang, G. Jiang, X. Dong, T. Cai, Z. Tian, Z. Di, G. Huang, X. Chen, E. Song, J. Cui, Y. Mei, *Proc. Natl. Acad. Sci* **2025**, *122*, 2500680122.
[12] Q. Zheng, J.-Q. Wang, W.-Q. Cao, H.-Z. Zhai, M.-S. Cao, *Adv. Funct. Mater.* **2025**, *35*, 2417972.
[13] H. Fu, K. Nan, W. Bai, W. Huang, K. Bai, L. Lu, C. Zhou, Y. Liu, F. Liu, J. Wang, M. Han, Z. Yan, H. Luan, Y. Zhang, Y. Zhang, J. Zhao, X. Cheng, M. Li, J. W. Lee, Y. Liu, D. Fang, X. Li, Y. Huang, Y. Zhang, J. A. Rogers, *Nat. Mater.* **2018**, *17*, 268.

[14] W. Huang, J. Zhou, P. J. Froeter, K. Walsh, S. Liu, M. D. Kraman, M. Li, J. A. Michaels, D. J. Sievers, S. Gong, X. Li, *Nat. Electron.* **2018**, *1*, 305.
[15] F. Gabler, D. D. Karnaushenko, D. Karnaushenko, O. G. Schmidt, *Nat. Commun.* **2019**, *10*, 3013.
[16] Y. Guo, B. Peng, R. Qiu, G. Dong, Y. Yao, Y. Zhao, Z. Zhou, M. Liu, *Adv. Funct. Mater.* **2023**, *33*, 2213668.
[17] L. Long, Q. Deng, R. Huang, J. Li, Z.-Y. Li, *Light Sci. Appl.* **2023**, *12*, 219.
[18] Y. Chen, Y. Lu, M. Liao, Y. Tian, Q. Liu, C. Gao, X. Yang, C. Shan, *Adv. Funct. Mater.* **2019**, *29*, 1906040.
[19] X. Zhou, Z. Tian, H. J. Kim, Y. Wang, B. Xu, R. Pan, Y. J. Chang, Z. Di, P. Zhou, Y. Mei, *Small* **2019**, *15*, 1902528.
[20] Z. Zhang, B. Wu, Y. Wang, T. Cai, M. Ma, C. You, C. Liu, G. Jiang, Y. Hu, X. Li, X.-Z. Chen, E. Song, J. Cui, G. Huang, S. Kiravittaya, Y. Mei, *Nat. Commun.* **2024**, *15*, 3066.
[21] Y. Jin, S. Xue, Y. He, *Adv. Mater. n/a*, 2500076.
[22] M. Calvo, A. E. Jakus, R. N. Shah, R. Spolenak, D. C. Dunand, *Adv. Eng. Mater.* **2018**, *20*, 1800354.
[23] Q. Geng, D. Wang, P. Chen, S.-C. Chen, *Nat. Commun.* **2019**, *10*, 2179.
[24] Z. Yan, F. Zhang, J. Wang, F. Liu, X. Guo, K. Nan, Q. Lin, M. Gao, D. Xiao, Y. Shi, Y. Qiu, H. Luan, J. H. Kim, Y. Wang, H. Luo, M. Han, Y. Huang, Y. Zhang, J. A. Rogers, *Adv. Funct. Mater.* **2016**, *26*, 2629.
[25] X. Ning, X. Yu, H. Wang, R. Sun, R. E. Corman, H. Li, C. M. Lee, Y. Xue, A. Chempakasseril, Y. Yao, Z. Zhang, H. Luan, Z. Wang, W. Xia, X. Feng, R. H. Ewoldt, Y. Huang, Y. Zhang, J. A. Rogers, *Sci. Adv.* **2018**, *4*, aat8313.
[26] J. A. Rogers, K. Yu, *Bioresorbable Silicon Electronics for Transient Implants*, US10925543B2 University of Illinois System, Illinois **2021**.
[27] M. Cho, J. Han, J. Suh, J. Kim, J. Ryu, I. Min, M. Sang, S. Lim, T. Kim, K. Kim, K. Kang, K. Hwang, K. Kim, E. Hong, M. Nam, J. Kim, Y. Song, G. Lee, I. Cho, K. Yu, *Nat. Commun.* **2024**, *15*, 2000.
[28] Y. Chen, M. Tan, R. Yang, C. K. W. Lee, H. Zhong, Y. Xu, Y. Huang, M. Tang, M. G. Li, *Adv. Funct. Mater.* **2024**, *34*, 2400090.
[29] I. S. Chun, A. Challa, B. Derickson, K. J. Hsia, X. Li, *Nano Lett.* **2010**, *10*, 3927.
[30] M. Li, W. Zhu, X. Li, H. Xu, X. Fan, H. Wu, F. Ye, J. Xue, X. Li, L. Cheng, L. Zhang, *Adv. Sci.* **2022**, *9*, 2201118.
[31] X. Lin, Y. Fang, L. Zhu, J. Zhang, G. Huang, J. Wang, Y. Mei, *Adv. Opt. Mater.* **2016**, *4*, 936.
[32] R. Songmuang, A. Rastelli, S. Mendach, O. G. Schmidt, *Appl. Phys. Lett.* **2007**, 90.
[33] J. Huang, C. You, B. Wu, Y. Wang, Z. Zhang, X. Zhang, C. Liu, N. Huang, Z. Zheng, T. Wu, S. Kiravittaya, Y. Mei, G. Huang, *Light Sci. Appl.* **2024**, *13*, 153.
[34] Y. Zhang, F. Zhang, Z. Yan, Q. Ma, X. Li, Y. Huang, J. A. Rogers, *Nat. Rev. Mater.* **2017**, *2*, 17019.
[35] J. A. Michaels, D. R. Wood, P. J. Froeter, W. Huang, D. J. Sievers, X. Li, *Adv. Mater. Interfaces* **2019**, *6*, 1901022.
[36] D. Jayachandran, N. U. Sakib, S. Das, *Nat. Rev. Electr. Eng.* **2024**, *1*, 300.
[37] H. Zhan, Y. Nie, Y. Chen, J. M. Bell, Y. Gu, *Adv. Funct. Mater.* **2020**, *30*, 1903841.
[38] H. Guo, Q. Zhang, W. Liu, Z. Nie, *ACS Appl. Mater. Interfaces* **2020**, *12*, 13521.
[39] D. Fu, K. Liu, T. Tao, K. Lo, C. Cheng, B. Liu, R. Zhang, H. A. Bechtel, J. Wu, *J. Appl. Phys.* **2013**, *113*, 043707.
[40] M. Loeblein, S. H. Tsang, M. Pawlik, E. J. R. Phua, H. Yong, X. W. Zhang, C. L. Gan, E. H. T. Teo, *ACS Nano* **2017**, *11*, 2033.
[41] T. Zhan, M. Xu, Z. Cao, C. Zheng, H. Kurita, F. Narita, Y.-J. Wu, Y. Xu, H. Wang, M. Song, W. Wang, Y. Zhou, X. Liu, Y. Shi, Y. Jia, S. Guan, T. Hanajiri, T. Maekawa, A. Okino, T. Watanabe, *Micromachines* **2023**, *14*, 2076.
[42] N. Sutherland, S. Marsh, G. Priestnall, P. Bryan, J. Mills, *Remote Sens.* **2023**, *15*, 2422.
[43] F. Menges, P. Mensch, H. Schmid, H. Riel, A. Stemmer, B. Gotsmann, *Nat. Commun.* **2016**, *7*, 10874.
[44] P. Löw, B. Kim, N. Takama, C. Bergaud, *Small* **2008**, *4*, 908.
[45] L. L. Noc, D. Dufour, M. Terroux, B. Tremblay, J. Lambert, L. Mercier, M. Morissette, C. Vachon, D. Tang, A. Bergeron, *In Infrared Technology and Applications*, *Vol. XXXVII*, SPIE, Bellingham, Washington, USA **2011**, p. 1185.
[46] C. Neumann, S. Reichardt, P. Venezuela, M. Drögeler, L. Banszerus, M. Schmitz, K. Watanabe, T. Taniguchi, F. Mauri, B. Beschoten, S. V. Rotkin, C. Stampfer, *Nat. Commun.* **2015**, *6*, 8429.
[47] D. Tuschel, *Raman thermometry* **2016**, *31*, 8.
[48] R. Songmuang, A. Rastelli, S. Mendach, C. Deneke, O. G. Schmidt, *Microelectron. Eng.* **2007**, *84*, 1427.
[49] B. J. Kip, R. J. Meier, *Appl. Spectrosc.* **1990**, *44*, 707.
[50] Y. Li, A. Fan, X. Zhang, X. Zhang, *Int. J. Heat Mass Transf.* **2023**, *216*, 124555.
[51] D.-W. Oh, C. Ko, S. Ramanathan, D. G. Cahill, *Appl. Phys. Lett.* **2010**, 96.
[52] M. Pan, J. Liu, H. Zhong, S. Wang, Z. Li, X. Chen, W. Lu, *J. Cryst. Growth* **2004**, *268*, 178.